Effect of micro-cracking on the electrical and self-sensing properties of an engineered cementitious composite under tensile straining

PAPER • **OPEN ACCESS**

Effect of micro-cracking on the electrical and self-sensing properties of an engineered cementitious composite under tensile straining

To cite this article: D Saraireh *et al* 2020 *IOP Conf. Ser.: Mater. Sci. Eng.* **930** 012054

Effect of micro-cracking on the electrical and self-sensing properties of an engineered cementitious composite under tensile straining

D Saraireh[1], B Suryanto[1]* and A Tambusay[1,2]

[1] Institute for Infrastructure and Environment, School of Energy, Geoscience, Infrastructure and Society, Heriot-Watt University, Edinburgh, United Kingdom.
[2] Department of Civil Engineering, Faculty of Civil, Planning and Geo Engineering, Sepuluh Nopember Institute of Technology, Surabaya, East Java, Indonesia.

*Corresponding author's e-mail: B.Suryanto@hw.ac.uk

Abstract. The piezo-resistive response of a relatively mature engineered cementitious composite (ECC) under tensile straining is investigated and compared with previous studies. In this work, tensile tests were performed on four dog-bone shaped ECC samples and during the loading process, electrical impedance measurements were undertaken over the frequency range 100Hz–1MHz to identify the bulk resistance (hence accurate evaluation of resistivity). At the same time, digital images of the front face of the dog-bone samples were recorded throughout the entire loading process to enable detailed crack width analysis to be taken after testing and to monitor micro-crack formation during testing, using the digital image correlation. It is shown that tensile straining resulted in an overall increase in impedance, but retained a similar overall profile with a weakly developed spur evident at the low-frequency side of the impedance spectrum and a circular arc at the high-frequency side. It is also shown that the fractional change in resistivity increases nonlinearly with strain and is related to the nature of micro-crack formation. Published values for fractional change in resistivity and its relation with strain were found to be in a large scatter and in this study, attention is therefore focused on the crack width distribution during loading.

1. Introduction

Concrete cracking can have a detrimental effect on the durability and long-term performance of concrete structures and appropriate measures must therefore be taken to control cracking. Various methods have been employed in this regard, ranging from altering the concrete mix composition (i.e. limiting the cement content, use of chemical admixtures) to providing a well-distributed embedded reinforcement and/or a construction joint; these measures are generally taken to ensure that cracking will not affect the serviceability and durability of reinforced concrete. Given that control of cracking is of practical importance and that crack formation can greatly accelerate the deterioration process in reinforced concrete and reduce service life [1-3], it is of common practice to undertake periodic visual (on-site) inspections to identify potential defects. However, this is not always possible as some damage may not be readily visible, thereby remaining undetected until advanced stages which would be costly to repair. Furthermore, whilst visual inspections are simple to perform and allow direct evidence to be gathered, it can only give a qualitative measure and hence little insight into the integrity of a structure [4]. A number of automated, structural health monitoring systems have been developed in this regard [5, 6] and these systems generally require the installation of an extensive network of sensors.

Recently, there has been a growing interest to use the concrete itself as a sensor due to its omnipresence in a structure [7]. At the same time, with increasing importance placed on producing durable concrete structures, there is also a growing interest in utilising fibre reinforcement as a means of more effective crack control. It is known that fibre additions into concrete can offer improvements in many of the mechanical properties of concrete such as enhanced toughness, reduced creep and shrinkage as well as improvements in the post-cracking behaviour. In this work, attention is given to a special type of fibre reinforced cement-based materials called the engineered cementitious composite (ECC) which is particularly known for its damage tolerant properties due to its high tensile strain capacity (in the order of a few percent) and superior crack width control (with crack width < 100μm commonly reported) [8-9]. As a cement-based material, ECC is shown to have a comparable electrical properties to a semi-conductor (10–10^5 Ωcm) [7]; the electrical properties of ECC could therefore be exploited to give a structure with self-monitoring capabilities with respect to internal damage and deformation under external loads.

With regard to damage sensing, work has predominantly focussed on the piezo-resistive properties (the resistivity change induced by mechanical strain) of ECC under tensile loading. To date, much of the work has studied these properties primarily through either d.c. or fixed-frequency a.c. resistivity measurements [7, 10-15]. In this paper, the a.c. electrical properties of ECC are investigated over a wide frequency range to identify the bulk electrical property more accurately. Detailed crack analyses through both visual (manual) observations and automated crack mapping technique (digital image correlation [16-18]) are also performed to provide supporting information in relation to the changes in electrical properties while under loading. The acquired electrical data are also compared with test data available in the literature [7,10-15] and a considerable scatter in published values is highlighted to call for the need for the development of a standardised test procedure.

2. Experimental Programme

2.1. Materials and mix proportion

The ECC mix used within the experimental program is presented in table 1. The binder comprised CEM I 52.5N Portland cement (PC) and fine fly-ash (Superpozz SV80), with a fly-ash/cement (FA/PC) ratios of 1.8. The water/binder (w/b) ratio was set as 0.28. Fine silica sand (RH110) with a mean grain size of 120μm was incorporated in the matrix at a sand/cement (S/C) ratio of 0.6 by mass. Polyvinyl alcohol (PVA) fibres were used at a dosage of 2% by volume. The fibres had an average length of 12mm and diameter of 39μm; the surface of which were coated with a thin layer of oiling agent (1.2% by weight). High-range water-reducing (HRWR) admixture was added at an dosage of 1% by cement weight.

Table 1. Summary of ECC mix and compressive strengths.

PC (kg/m^3)	FA (kg/m^3)	S (kg/m^3)	HRWR (kg/m^3)	PVA (kg/m^3)	w/b	Compressive strength (MPa)		
						28 days	90 days	180 days
454	818	273	4.54	2.6	0.28	40.3	53.1	65.5

Notes: PC: CEM I 52.5N; FA: fly ash; S: sand; HRWR: high-range water-reducing admixture; and PVA: polyvinyl alcohol.

2.2. Test specimens, fabrication and curing

A 10-litre Hobart planetary motion mixer was used to produce a total of 13 samples: four dog-bone shaped samples to determine the mechanical and electrical properties under tensile loading; and nine cubes to determine the compressive strength at 28^{th}, 90^{th} and 180^{th} days after casting. Immediately after mixing, the fresh mix was placed into the corresponding moulds (Plexiglas moulds for the dog-bone samples and three-gang steel moulds for the cubes). All samples were then covered with cling film and allowed to cure for 24 h in a temperature controlled laboratory (21±2°C) before being demoulded and stored in a curing tank. After two weeks, two electrodes consisting of fine metal wire were wrapped securely at the opposing ends of the narrower portion of each dog-bone sample, as presented in figure

1. These wires were covered with several layers of silver-loaded conductive paint to seal any gaps and ensure intimate bonding with the sample. When the paint was fully dry, all dog-bone samples were returned to the curing tank until required for testing (180 days after casting).

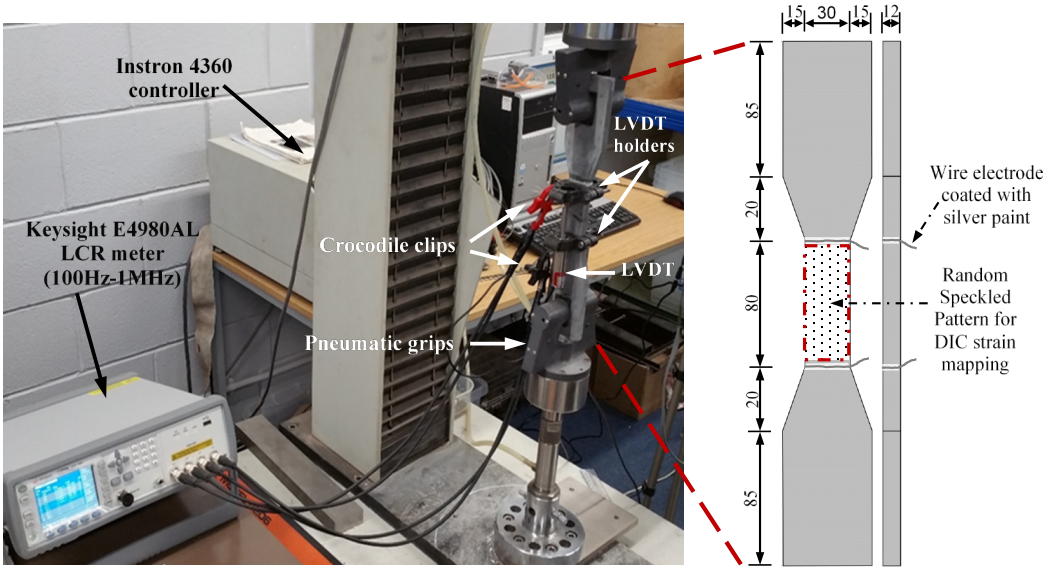

Figure 1. Dog-bone sample during tensile testing displaying the test setup and equipment used for testing. The dimensions of the dog-bone sample (in mm) are provided for clarity.

2.3. Testing equipment and procedures

A 100kN Instron machine was used to perform direct tensile tests. Each dog-bone sample was aligned in the machine and clamped at both ends using pneumatic grips. Two linear variable displacement transducers (LVDTs) were used to measure the strain within the centre (narrower) region and these transducers were fixed at the opposing ends of this monitoring portion, one at each side of the sample, by means of lightweight plastic mounting blocks. Bluehill 2 software was used to manage the overall running of the experiment and log data from the load cell. Tensile stresses were determined by dividing the load cell readings with the cross-sectional area of the narrower section. In addition to this, a 16-bit 8-channel multifunction USB data acquisition system was used to log LVDT readings which were then converted to tensile strains using a calibration factor. These data were then used to plot the tensile stress-strain relation for each sample. All measurements were taken at a rate of 1Hz.

In addition to stress and strain measurements, electrical impedance measurements were undertaken during the loading process using an E4980AL precision LCR meter. This was done by connecting the pair of wire electrodes to four, individually screened, coaxial cables, with connection at the wire via an alligator clip. The LCR meter was controlled by a Desktop PC using LabVIEW virtual instrument. For each sample, electrical measurements were taken every three seconds at thirteen spot frequencies over the frequency range 100Hz–1MHz, covering 100Hz, 200Hz, 500Hz, 1kHz, 2kHz, 5kHz, 10kHz, 20kHz, 50kHz, 100kHz, 200kHz, 500kHz and 1MHz. These frequencies were chosen based on the time needed to perform a single full sweep measurement (slightly less than 3 seconds to complete).

To monitor micro-crack formation during testing, the digital image correlation technique was used. Prior to testing, the front surface of each dog-bone sample was painted white and then marked with random dotted patterns using a black marker (see figure 1). Once the sample was in position in the Instron machine, an 18.4MP Nikon J4 mirrorless digital camera was placed on a stable tripod in front of the sample. Digital images were then acquired at every 0.1mm extension to monitor the evolution of micro-cracks with increasing strain. This image acquisition was done wirelessly through a wireless mobile utility application installed on a mobile phone and this was specifically done to prevent camera movement which would render accuracy. Once the test was completed, the images were downloaded onto a Desktop PC and processed using a DIC software Ncorr [16-18] to follow the formation and propagation of micro-cracking during the entire loading process. In addition to this digital crack

mapping, the crack pattern at various stages of loading was manually observed using the ImageJ software in order to measure individual crack widths, more accurately, and crack number.

3. Results and discussion

3.1. Complex impedance and bulk resistance

The typical complex impedance spectra for two dog-bone samples (DB2 and DB3) during tensile testing are presented in figures 2(a) and (b), respectively, as a Nyquist plot. Data markers represent the response acquired at the 13 spot frequencies (see section 2.3), with frequency increasing from right-to-left across each spectrum. In this figure, although measurements were obtained every 3 seconds, for clarity, only the response at 1% strain increment is presented (an example of a full impedance response over a 3-sec cycle during tensile straining is available in [19]). It is immediately apparent from figures 2(a) and (b) that during the entire loading process, the two samples displayed a typical impedance response with three distinct regions always evident:

(i) an arc on the high-frequency (left-hand) side of the spectrum;
(ii) a short intermediate plateau; and
(iii) a weakly developed spur at the low-frequency (right-hand) side of the spectrum.

The low-frequency spur is visible in the Nyquist diagrams presented due to polarization at the electrode/specimen interface and represents part of a much larger arc which would only become apparent at lower frequencies (viz, <<100Hz) and [20,21]. The arc represents the overall bulk impedance response of the sample. The bulk resistance of the test sample, R (Ω), which is related to ionic conduction processes [22], can be obtained from the intercept of the low-frequency end of the arc with the real axis.

With reference to figures 2(a) and (b), it is evident that tensile straining resulted in the entire impedance response being gradually displaced to the right, indicating an overall increase in impedance with increasing strain. This gradual increase in the impedance is due to the formation and widening of multiple micro-cracks during testing [19] (further presented and discussed in the section below).

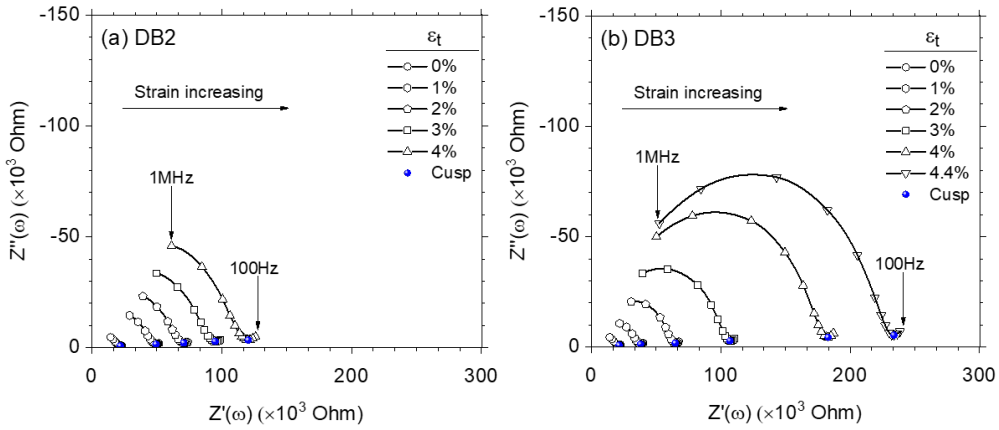

Figure 2. Typical complex impedance response during tensile loading for (a) DB2 and (b) DB3 samples. The cusp points are highlighted with circular (solid) data marker.

In this work, the minimum point within the intermediate region (the cusp point) is used to estimate the bulk resistance of the ECC samples due to its close location with the projected intercept of the low-frequency end of the arc with the real axis. In all samples, the frequency at which the cusp-point occurs was observed to occur at ~500Hz. Due to the amount of data collected, only the response at this spot frequency will be presented in the next section and discussed.

3.2. Fractional change in resistivity

The fractional change in resistivity (FCR) is a parameter that has been widely used in previous studies to highlight the self-monitoring feature of a material under loading, including various versions of ECC

under tensile loading (see, for example, [7, 10-15]). The bulk resistivity, ρ (Ωm), can be determined by relating the bulk resistance obtained at the cusp point as discussed above to the electrode configuration and sample geometry through the relationship,

$$\rho = \frac{RA}{L} \tag{1}$$

where A is the cross-sectional area of the narrower (central) section of the dog-bone sample (approximately $0.03\times0.012\text{m}^2$); L is the measured distance between the two electrodes (approximately 0.08m); and A/L is the geometrical constant (/m). Since the electrodes used in this study did not cover the whole cross-section of the central region, current in regions close to the opposing ends of the central region would not flow across the full cross-sectional area and this may affect the value of geometry constant above. However, considering the relatively large length-to-depth ratio over the central section, this simple method of determination of geometrical constant could be considered sufficiently accurate. Alternatively, the geometrical constant can also be evaluated through a calibration procedure using the four-point method [23]. The FCR can be computed by normalising the change in resistivity after the start of testing, $\Delta\rho$, by the resistivity at zero strain (at the start of the test), ρ_o, through the following relationship,

$$\text{FCR} = \frac{\Delta\rho}{\rho_\text{o}} \tag{2}$$

Given that the change in length during testing is quite small (generally less than 5%), in this work, it is assumed that the geometric constant before and after deformation remains constant. This will have the effect of removing the need of calculating the resistivity; the bulk resistance can therefore be directly used in equation (2) in place of bulk resistivity. In addition to FCR, it is also possible to check the sensitivity of the material to mechanical strain and for this, the apparent gauge factor, GF, could be calculated through the following relationship,

$$\text{GF} = \frac{\Delta\rho/\rho_0}{\Delta\varepsilon_\text{t}} \tag{3}$$

where $\Delta\varepsilon_\text{t}$ is the change in tensile strain during testing.

Figure 3(a) displays the FCR at the cusp-point frequency (~500Hz) for all dog-bone samples, together with the tensile stress-strain response obtained from the same samples. It is evident that the FCR plots exhibit a nonlinear increase with strain, with the FCR value at failure of 19.7, 4.6, 9.7 and 17.2 for DB1, DB2, DB3 and DB4 samples, respectively. The increase in FCR is associated with the progressive development of micro-cracks during the strain-hardening phase. It is interesting to note that the FCR values for DB2 sample at 4% strain are comparable those reported earlier by [7, 15] who conducted similar tests on relatively young specimens (28 days of curing). However, the rest of the samples all attained much higher values of FCR (~11.7 (DB1), ~7.3 (DB3) and ~9.9 (DB4)) which would indicate higher sensitivity to tensile straining (or crack formation). This could be associated with the process of micro-crack development and the distribution of the micro-cracks during loading. It is anticipated that as the capillary pores within the ECC matrix break down (as being intercepted with a micro-crack), the crack space may be partially filled by pore-water thereby creating a water bridging conduction path across the micro-crack. With increasing time, however, the amount of free water within the ECC matrix could be expected to decrease due to the reduction in overall porosity resulting from on-going cement hydration and pozzolanic reaction. As a result, less water bridging effects could be expected in a mature ECC sample, as in the samples tested in this study. In addition to this aspect, it was observed that the crack widths were relatively large and this could also contribute to the enhancement in sensitivity.

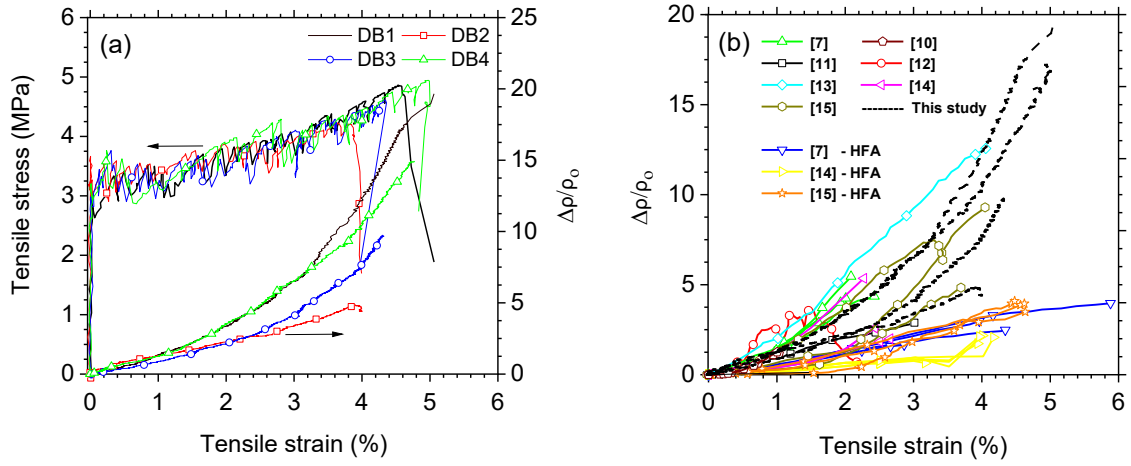

Figure 3. (a) The FCR for D1-D4 samples, together with the tensile stress-strain response; (b) comparison of the obtained FCR values with data reported in previous studies [7,10-15].

Figure 3(b) provides a summary of the FCR values of different versions of ECCs obtained from the literature [7,10-15]. It is apparent that there is clearly a wide scatter in published FCR values for similar ECCs and the values obtained in this study are within the range of the published values. With regard to the apparent slope of the FCR curve at 1% (i.e. the apparent GF over the initial 1% strain), this varies from only about 8 [15] and 15 [14] to as high as approximately 170 in [7]; 200 in [13]; and 260 in [12], with higher slope values indicating higher sensitivity. It is interesting to note that in cases with relatively low slope values, high volume of fly-ash (HFA) was used in the mix formulation and this type of ECC normally exhibits extremely small crack width, as reported in [7]. The large scatter in data could, therefore, be partly attributed to differences in crack width. It is also interesting to note that the FCR values obtained in this study are very similar to those reported by [15]. From figure 3(b), it is clear that there has been a few data published at strains levels of greater than approximately 4% and the data obtained in this paper could be useful in this regard. Given that the large variations in FCR values are likely related to the distribution and pattern of the micro-cracks, the number and width of the individual micro-crack during loading are presented and discussed below.

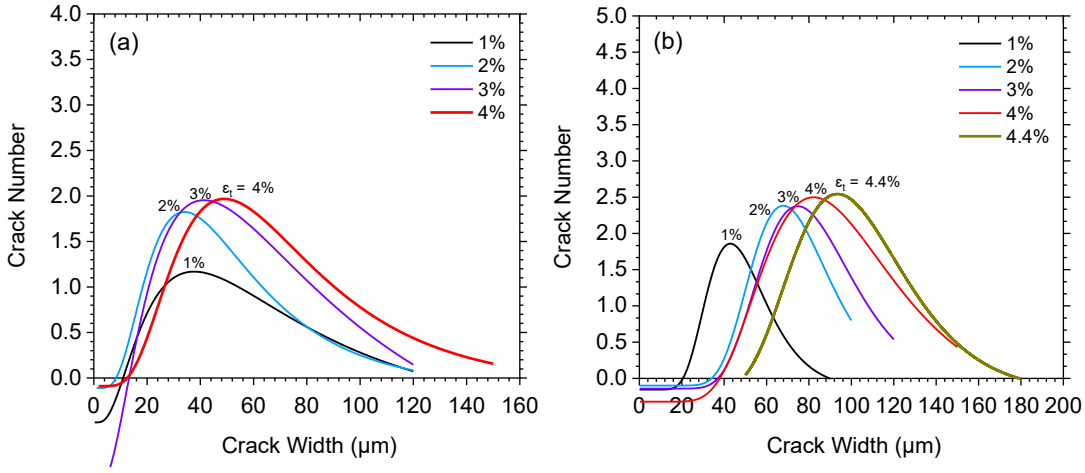

Figure 4. Crack distribution observed at varying strain levels for (a) DB2 and (b) DB3 samples.

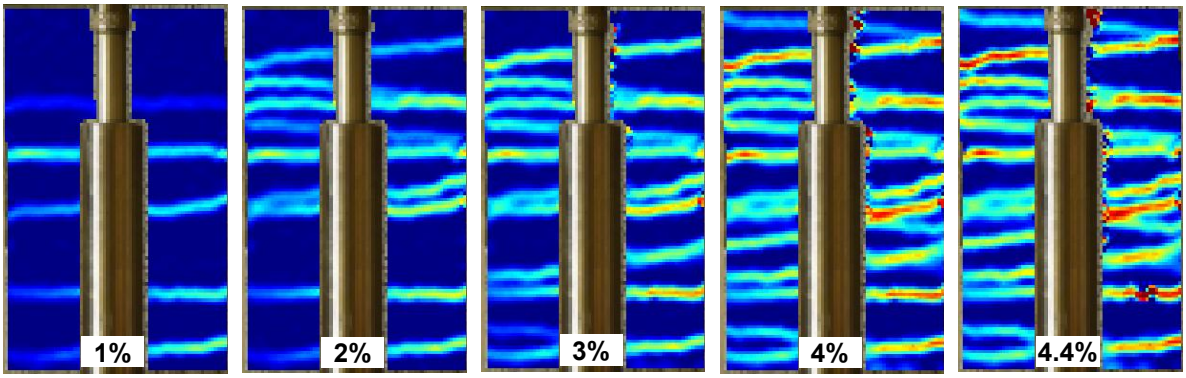

Figure 5. Progressive development of longitudinal strains obtained using the DIC for DB3 sample.

Figures 4(a) and (b) present the crack number-crack width relation, with the best-fit lognormal distribution curves presented for DB2 and DB3 samples, respectively. With reference to figure 4(a), it is evident that there is a progressive displacement of the curve upward, indicating an increase in crack number, and this occurs within the same crack width range (between 10μm and 120μm). At strain levels larger than 3%, however, the crack distribution curve starts to displace to the right while the peak value remains the same which is indicative of crack widening (without an increase in crack number). It is interesting to note that the crack width distribution of sample DB3 (see figure 4(b)) exhibits a different trend, displaying a continuous upward and progressive displacement to the right-hand-side up to 4% strain, when only progressive displacement to the right is observed. This would imply that there was a continuous increase in crack number and width of micro-cracks at strain levels less than 4%. Beyond that, only crack widening is operative. This observation agrees well with the DIC strain maps depicted in figure 5 which clearly display that there was indeed a progressive increase in crack number throughout the entire loading process, in particular between 1% and 2% strains.

4. Concluding remarks

1. The complex impedance response of cracked ECC during tensile loading displayed a classic impedance responses comprising an arc at the high-frequency end and a spur (only weakly developed) at the low-frequency end. Tensile straining was found to affect both the resistive and reactive components of the complex impedance, with both components shown to increase with increasing strain.
2. There is a nonlinear relationship between tensile strain and the fractional change in resistivity (FCR). The increase in FCR is shown to be gradual, due to the progressive micro-cracks formation within the ECC matrix.
3. Micro-cracks were found to exert an influence on the fractional change in resistivity, with the sensing sensitivity to tensile deformation increasing with increasing crack width.
4. There is a wide scatter in published FCR values for ECCs. Although the values obtained in this study are within the range of the published values, the authors want to call for the need for the development of a standardised test procedure to enable the assessment of the electrical and hence the self-sensing properties of ECC more accurately.

Overall, it has been shown that there is a close relationship between the electrical properties of ECC and crack width and, as such, the electrical properties of ECC could be further exploited as an alternative means of assessing the crack width in ECC (and hence in the quality control of an ECC mix). Although not considered as a variable in the present work, moisture could also be expected to exert a dominant influence on the measured resistivity and work is continuing in this respect.

Acknowledgements

The authors wish to acknowledge the financial support of the Engineering and Physical Sciences Research Council, United Kingdom (Grant EP/N028597/1), Kuraray Japan and Kuraray GmbH for

supplies of PVA fibres, and BASF UK for supplies of water reducers. DS also acknowledges the financial support provided by Heriot-Watt University.

References

[1] Alyousif A, Lachemi M, Yıldırım G, Aras G H and Sahmaran M S 2015 Influence of cyclic frost deterioration on water sorptivity of microcracked cementitious composites *J. Mater. Civ. Eng.* 28 04015159.
[2] Kobayashi K, Le Ahn D and Rokugo K 2016 Effects of crack properties and water-cement ratio on the chloride proofing performance of cracked SHCC suffering from chloride attack *Cem. Concr. Compos.* **69** 18–27.
[3] Wang J, Basheer PM, Nanukuttan SV, Long AE and Bai Y 2016 Influence of service loading and the resulting micro-cracks on chloride resistance of concrete *Constr. Build. Mater.* **108** 56–66
[4] Hoult N, Fidler P, Hill P and Middleton C 2010 Long-term wireless structural health monitoring of the Ferriby road bridge *J. Bridge Eng.* **15** 2 153–9.
[5] Brownjohn J M W 2007 Structural health monitoring of civil infrastructure *Philos. Trans. R. Soc. Lond. A* **365** 1851 589–622.
[6] Abé M and Fujino Y (2017) Monitoring of long-span bridges in Japan. *P. I. Civil Eng.–Civil Eng.* **170** 3 135–44.
[7] Ranade R, Zhang J, Lynch J and Li V 2014 Influence of micro-cracking on the composite resistivity of Engineered Cementitious Composites *Cem. Concr. Res.* **58** 1–12.
[8] Li V C 2008 Engineered cementitious composites (ECC)–material, structural, and durability performance *Concrete Construction Engineering Handbook* ed E G Nawy (Michigan: CRC Press) chapter 24 pp 1–48.
[9] Suryanto B, Buckman J O, Thompson P, Bolbol M and McCarter W J 2016 Monitoring micro-crack healing in an engineered cementitious composite using the environmental scanning electron microscope *Mater. Charact.* **119** 175–85.
[10] Yıldırım G, Öztürk O, Al-Dahawi A, Ulu A A and Sahmaran M S 2020 Self-sensing capability of Engineered Cementitious Composites: Effects of aging and loading conditions *Constr. Build. Mater.* **231** 117132.
[11] Hou T C and Lynch J P 2005 Conductivity-based Strain Monitoring and Damage Characterization of Fiber Reinforced Cementitious Structural Components *In: Proc. of SPIE 12th Annual International Symposium on Smart Structures and Materials* pp 6-10.
[12] Lin V, Li M, Lynch J and Li V 2011 Mechanical and Electrical Characterisation of Self-sensing Carbon Black ECC *Proc. of SPIE* **7983** pp 1-12.
[13] Suryanto B, McCarter W J, Starrs G, Wilson S A and Traynor R M 2015 Smart cement composites for durable and intelligent infrastructure *Procedia Eng.* **125** 796–803.
[14] Huang Y, Li H and Qian S 2018 Self-sensing properties of engineered cementitious composites *Constr. Build. Mater.* **174** 253–62.
[15] Deng H and Li H 2018 Assessment of self-sensing capability of Carbon Black Engineered Cementitious Composites *Constr. Build. Mater.* 1**73** 1–9.
[16] Ncorr v1.2: Open source 2D-DIC Matlab software http://www.ncorr.com/
[17] Suryanto B, Tambusay A and Suprobo P 2017 Crack mapping on shear-critical reinforced concrete beams using an open source digital image correlation software *Civ. Eng. Dimens.* **19** 2 93–8
[18] Tambusay A, Suryanto B and Suprobo P 2020 Digital image correlation for cement-based materials and structural concrete testing *Civ. Eng. Dimens.* **22** 1 6–12.
[19] Saraireh D, Walls S, Suryanto B, Starrs G and McCarter W J 2017 The influence of multiple micro-cracking on the electrical impedance of an engineered cementitious composite *Proc. Int. Conf. on Strain-Hardening Cement-Based Composites* (Dordrecht: Springer) pp 292–9.
[20] McCarter W and Brousseau R 1990 The A.C. response of hardened cement paste *Cem. Concr. Res.* **20** 6 891–900.

[21] Suryanto B, McCarter W, Starrs G and Ludford-Jones G 2016 Electrochemical immittance spectroscopy applied to a hybrid PVA/steel fiber engineered cementitious composite *Mater. Des.* **105** 179–89.
[22] Whittington H W, McCarter J and Forde M C 1981 The conduction of electricity through concrete *Mag. Concr. Res.* 33 114 48–60.
[23] McCarter W J, Taha H M, Suryanto B and Starrs G 2015. Two-point concrete resistivity measurements: interfacial phenomena at the electrode–concrete contact zone. *Meas. Sci. Technol.* **26** 8 085007.